High-Efficiency Wireless Integrated On-Board Charger System Using Partial Power Conversion

Muxing Wu, *Student Member, IEEE*, Io-Wa Iam, and Chi-Seng Lam, *Senior Member, IEEE*

***Abstract*—This article proposes a wireless integrated on-board charger (WiOBC) for electric vehicles based on partial power conversion (PPC), which can simultaneously charge the high-voltage battery (HVB) and the auxiliary system (AS) with high efficiency. The proposed PPC-WiOBC can operate in two modes: 1) charging mode and 2) driving mode. During charging mode, a dual decoupled four-coil system is utilized to charge the HVB with a constant-current or constant-voltage charging profile and provide a constant dc voltage for AS. The surplus power will flow through the AS to the HVB via an auxiliary dc–dc converter. In driving mode, the auxiliary dc–dc converter operates backwards and the HVB supplies power to the AS. To meet high-efficiency and bidirectional operation requirements, an auxiliary *LC-LLC* multiresonant dc–dc converter, incorporating an additional inductor is introduced. A power ratio δ of the PPC is also introduced to ensure high efficiency. Finally, a comprehensive system parameter design of the PPC-WiOBC is proposed. Experimental results from a scale-down 1 kW experimental platform verify the performance of the proposed PPC-WiOBC, with output voltage ranges from 264 V to 402 V, a peak efficiency of 94.1%, and efficiency >87.1% throughout the whole charging profile, which is superior to the conventional wireless OBC solutions.**

***Index Terms*—Electric vehicle, integrated on-board charger, multiresonant dc–dc converter, partial power conversion, wireless power transfer.**

NOMENCLATURE

Abbreviations

OBC	On-board charger.
iOBC	Integrated on-board charger.
WOBC	Wireless on-board charger.
WiOBC	Wireless integrated on-board charger.
WPT	Wireless power transfer.
PPC	Partial power conversion.
HVB	High-voltage battery.
AS	Auxiliary system.
CC/CV	Constant-current or constant-voltage.
EV	Electric vehicle.
LDC	Low-voltage dc–dc converter.
HV-Rec	High-voltage rectifier.
LV-Rec	Low-voltage rectifier.

Indices

δ	Power ratio.
n_1	High-voltage side coil ratio.
n_2	Low-voltage side coil ratio.
f_w	Inverter switching frequency.
T_d	Inverter switching dead time.
n	*LC-LLC* transformer turns ratio.
f_s	*LC-LLC* switching frequency.
T_{dL}	*LC-LLC* switching dead time.
ω_s	*LC-LLC* angular switching frequency.
f_{r1}	First series resonant frequency.
f_{r2}	Second series resonant frequency.
f_{rs}	Series-resonant frequency ($f_{rs} = 1/(2\pi(L_s/C_s)^{1/2})$).
F_x	Normalized switching frequency ($F_x = f_s/f_{rs}$).
f_{rm}	L_{m1} resonant frequency ($f_{rm} = 1/(2\pi((L_s+L_{m1})/C_s)^{1/2})$).
F_{rm}	Normalized L_{m1} resonant frequency ($F_{rm} = f_{rm}/f_{rs}$).
f_{rp}	Antiresonant frequency ($f_{rp} = 1/(2\pi(L_p/C_p)^{1/2})$).
F_{rp}	Normalized antiresonant frequency ($F_{rp} = f_{rp}/f_{rs}$).
Z_{rs}	Series-resonant characteristics impedance ($Z_{rs} = (L_s/C_s)^{1/2}$).
Z_{rp}	Antiresonant characteristics impedance ($Z_{rp} = (L_p/C_p)^{1/2}$).
m_1	*LC-LLC* forward inductors ratio ($m_1 = L_{m1}/L_s$).
m_2	*LC-LLC* backward inductors ratio ($m_2 = L_{m2}/L_s$).
γ	*LC-LLC* series/antiresonant inductors ratio ($\gamma = L_p/L_s$).

Received 12 November 2024; accepted 5 January 2025. Date of publication 10 January 2025; date of current version 26 February 2025. This work was supported in part by the Science and Technology Development Fund, Macau SAR (FDCT) under Grant 0050/2024/ITP2, Grant 0015/2022/AMR, Grant 0027/2021/A1, and Grant 004/2023/SKL and in part by the University of Macau under Grant MYRG-GRG2024-00086-IME and Grant MYRG-GRG2023-00167-IME. Recommended for publication by Associate Editor B. K. Lee. *(Corresponding author: Chi-Seng Lam.)*

Muxing Wu and Chi-Seng Lam are with the State Key Laboratory of Analog and Mixed-Signal VLSI, University of Macau, Macau 999078, China, also with the Institute of Microelectronics, University of Macau, Macau 999078, China, and also with the Department of Electrical and Computer Engineering, Faculty of Science and Technology, University of Macau, Macau 999078, China (e-mail: cslam@um.edu.mo, c.s.lam@ieee.org).

Io-Wa Iam is with the State Key Laboratory of Analog and Mixed-Signal VLSI, University of Macau, Macau 999078, China, and also with the Institute of Microelectronics, University of Macau, Macau 999078, China.

Color versions of one or more figures in this article are available at https://doi.org/10.1109/TPEL.2025.3528130.

Digital Object Identifier 10.1109/TPEL.2025.3528130

I. INTRODUCTION

EVS have emerged as a crucial mode of transportation for consumers [1]. However, the primary impediments to their advancement are their limited range and extended charging duration [2], [3]. Addressing these challenges is essential to accelerate widespread EV adoption.

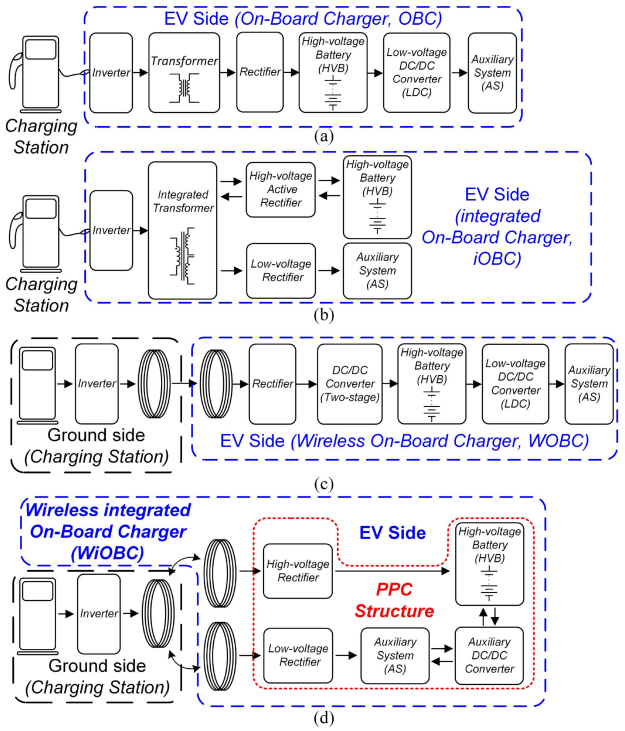

Fig. 1. EV on-board charger (OBC) system. (a) Conventional OBC [4]. (b) iOBC [8]. (c) Conventional two-stage WOBC [22]. (d) Proposed PPC-WiOBC.

One promising approach to mitigate these issues is to develop high-efficiency chargers for the mainstream 400 V and 800 V battery voltage configuration employed in EVs. Conventional OBC systems, as illustrated in Fig. 1(a), use an isolated dc–dc converter (comprising of inverter, transformer, and rectifier) to supply power to the HVB, and then employ another LDC to supply power to the AS [4], [5], [6]. While this approach ensures efficient HVB charging and AS operation, it necessitates isolation among the HVB, AS, and charging stations to mitigate potential leakage current issues [7]. Consequently, these systems tend to have larger volumes and higher component costs due to the isolated nature of the OBC and LDC. To improve power density, iOBC structures have been proposed, as depicted in Fig. 1(b). This approach employs a multiwinding transformer to simultaneously transfer power to the HVB and AS during the charging mode [8], [9], [10]. However, during the driving mode, the HVB supplies power to the AS through the backward operation of the HV-Rec circuit and LV-Rec circuit. This shared transformer structure results in circulating current loops during driving mode, leading to additional power losses and reduced efficiency.

WPT technology necessitates only a receiving coil in the EV, thereby obviating power losses attributable to the circulating current loop during driving mode. Furthermore, owing to complete isolation, it mitigates potential hazards associated with electrical damage and shock resulting from physical cords between the charging station and the EV [11], [12], [13]. The CC/CV charging profile commonly used in EV battery charging requires the wireless on-board charger (WOBC) to operate

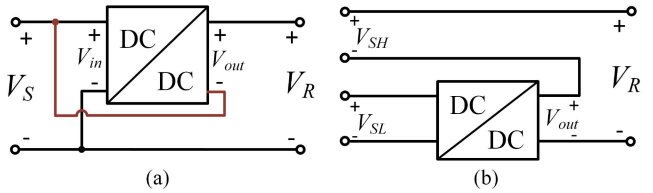

Fig. 2. PPC topology type including (a) single-source and (b) double-source.

within a wide output voltage range [14]. In the WPT systems, two types of control methods exist for a single-stage OBC, including transmitter control and receiver control. The transmitter control utilizes the conventional control mode, enabling wide output range modulation to be achieved [15], [16], [17], [18]. However, these methods rely on feedback wireless communication, which increases the risk of instability during charging [19]. The regulation capability of receiver control is relatively limited, which may result in hard switching [20] or alter the resonance state [21]. Hence, a two-stage regulation structure incorporating an additional dc–dc converter (two-stage) is often employed to address the limited regulation capability issue, as illustrated in Fig. 1(c) [22]. Due to the extra power stage, significantly degrades the system's efficiency and increases the system's complexity and cost.

To mitigate the efficiency losses associated with two-stage structures, the PPC technique has been proposed in [23], the structure is depicted in Fig. 2(a). The PPC technique involves processing only a fraction of the total power through an auxiliary dc–dc converter, allowing the majority of the power to flow directly to the load without regulation. The reduction in the power requiring regulation leads to an enhancement in overall efficiency. Recently, the PPC topology concept has been implemented into OBC system applications for EVs. In [24], a cascade output design based on PPC technology has been proposed, incorporating a buck postregulator to meet the battery charging requirements, the structure is depicted in Fig. 2(b). This approach demonstrates improved charging efficiency compared with a conventional charging structure. The work in [25] further expanded the output range by implementing a multistage parallel connection based on the cascade as an OBC for EV. The double-source PPC is also introduced in wireless charging, such as a current-split double-source PPC proposed in [26], in which the main path adopts voltage-type compensation, while the auxiliary path adopts current-type compensation. The power is split by a double D quadrature (DDQ) coil. A magnetic integrated transformer is utilized to provide two power paths, with only a single coil at the receiver, increasing the compactness of the charging system [27]. Nevertheless, it is noteworthy that in [26] and [27], neither the low-voltage output side of the PPC nor the EV auxiliary system was analyzed. Furthermore, although the PPC technique was employed to improve charging efficiency, the lack of a systematic design approach considering power ratio constraints and converter parameters has limited its practical application.

To address the aforementioned drawbacks of the existing solutions, this article proposes a WiOBC based on a partial power conversion (PPC-WiOBC) system for EVs, as illustrated

in Fig. 1(d). By employing a multiport wireless coil and forming a double-source PPC structure, the PPC-WiOBC system can simultaneously charge the HVB and provide a constant dc voltage for the AS with high efficiency through the whole charging profile compared to the conventional approaches. Moreover, the driving mode can be achieved through the backward operation of the auxiliary dc–dc converter. The main contributions of the proposed PPC-WiOBC system are summarized as follows.

1) In charging mode, a dual decoupled four-coil for the PPC-WiOBC system is designed to simultaneously charge the HVB and provide a constant dc voltage for the AS with less regulation power stage than the conventional wireless OBC, thus reducing power losses.
2) In driving mode, the auxiliary dc–dc converter operates backwards and the HVB supplies power to the AS.
3) A maximum power ratio δ constraint between the low-voltage side and high-voltage side is designed for the PPC, facilitating subsequent parameter design for high-efficiency operation.
4) A bidirectional *LC-LLC* multiresonant dc–dc converter with an antiresonance symmetrical resonant tank is introduced for the PPC-WiOBC, supporting an extremely wide output voltage range, and both charging and driving modes.
5) To further improve the overall system efficiency, a comprehensive system parameter design approach is proposed based on the high-efficiency region.

The rest of this article is organized as follows. Section II analyzes the proposed PPC-WiOBC system architecture and its operation modes, and the high-efficiency constraint region for the PPC operation is also derived. In Section III, the circuit structure and control schemes are analyzed in detail. Additionally, a comprehensive system parameter design process incorporating the PPC high-efficiency constraints is proposed to determine the system parameters. Section IV presents the experimental validation and an efficiency comparison between the proposed PPC-WiOBC system and the conventional two-stage WOBC system. Finally, Section V concludes this article.

II. Analysis of Proposed PPC-WiOBC System

A. Operating Modes of the Proposed PPC-WiOBC System

From the proposed PPC-WiOBC system, as shown in Fig. 1(d), during charging mode, the auxiliary dc–dc operates in forward mode, facilitating two power paths: PathI P_H and PathII P_L, to realize the PPC function, as depicted in Fig. 3(a). The outputs of the high-voltage side and low-voltage side rectifiers HV-Rec and LV-Rec at the receiver side are designed as CV sources. HV-Rec is directly connected to the HVB, while LV-Rec is connected to the EV's AS and the input of the auxiliary dc–dc converter. V_{oH} and V_{oA} is the output voltage of HV-Rec and LV-Rec. V_{oL} is the output voltage of auxiliary dc–dc converter. V_{oB} is the output voltage of system. I_{oC} is the charging current. The auxiliary dc–dc converter handles all output regulation functions.

During the driving mode, the HVB provides power to the AS through HV-Rec, in which the auxiliary dc–dc is operating

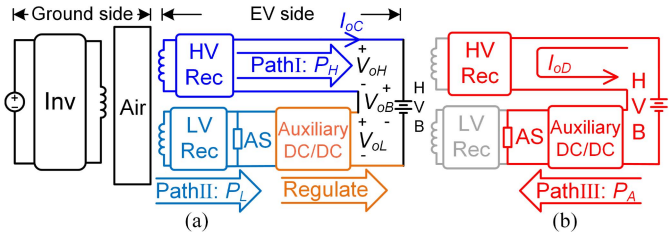

Fig. 3. (a) Charging mode and (b) driving mode of the proposed PPC-WiOBC system.

in backward mode. In this case, HV-Rec requires two active switches to enable the power Path III P_A. I_{oD} is the discharge current of HVB.

B. Circuit Architecture of Proposed PPC-WiOBC System

The circuit architecture of the proposed PPC-WiOBC is shown in Fig. 4(a), where L_{P1} and L_{P2} are the transmitter coils and L_{S1} and L_{S2} are the receiver coils of the dual decoupled four-coil system, the mutual inductances are denoted as M_{P1S1} and M_{P2S2}, which will be discussed in Section III-A. C_{P1}, C_{P2}, C_{S1}, and C_{S2} are the compensation capacitors of two series/series (S/S) compensation structures.

The transmitter side consists of an inverter circuit formed by switches S_1–S_4. On the receiver side, a rectifier circuit for the HV-Rec is formed by diodes D_1 and D_2, and switches S_5 and S_6. Another rectifier circuit for the LV-Rec is formed by diodes D_3 and D_4 and switches S_{15} and S_{16}. C_{oH} and C_{oA} are the filter capacitor of HV-Rec and LV-Rec sides, respectively. The regulation stage of the PPC-WiOBC employs a bidirectional *LC-LLC* multiresonant isolated dc–dc converter. This converter comprises switches S_7–S_{14}, series resonant component L_s and C_s, antiresonant component L_p and C_p, an additional inductance L_{m2}, and filter capacitor C_{oL}. The design and operation of this dc–dc converter will be discussed in Section III-C.

During the charging mode operation, S_5 and S_6 function as diodes to perform rectification in the circuit. The auxiliary dc–dc converter operates in forward mode, with S_7–S_{10} operating as an inverter and S_{11}–S_{14} operating as a rectifier.

During the driving mode operation, S_5 and S_6 remain turn-ON, forming a path for discharging the HVB. The magnetizing inductance L_{m2} becomes active, and the roles of the switches are reversed. S_7–S_{10} operates as a rectifier, while S_{11}–S_{14} functions as an inverter, enabling bidirectional power flow.

C. High-Efficiency Constraints for PPC Structure

The PPC technique is based on the principle of power division, comprising direct power PathI P_H and regulate power PathII P_L, as shown in Fig. 5(a). The majority of the power flows through PathI directly to the load, while a small portion of the power is regulated by the auxiliary dc–dc in PathII. By reducing the regulated power in PathII, the power losses P_{Loss} of the system can be significantly decreased, thereby improving the system efficiency. Furthermore, the power rating requirement for the auxiliary dc–dc converter is reduced due to the lower regulated power.

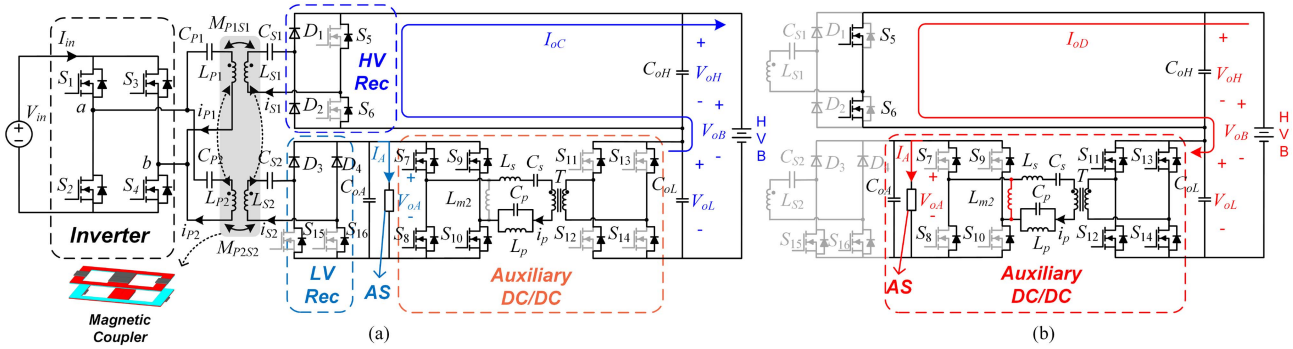

Fig. 4. Circuit architecture of the proposed PPC-WiOBC system during. (a) Charging mode. (b) Driving mode.

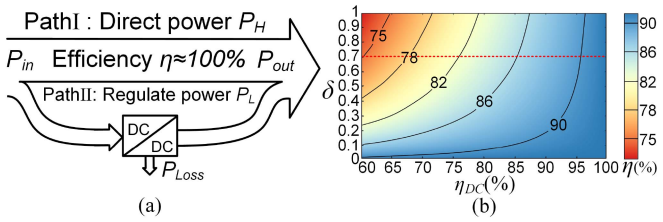

Fig. 5. (a) PPC power flow diagram and (b) proposed PPC-WiOBC system efficiency contour.

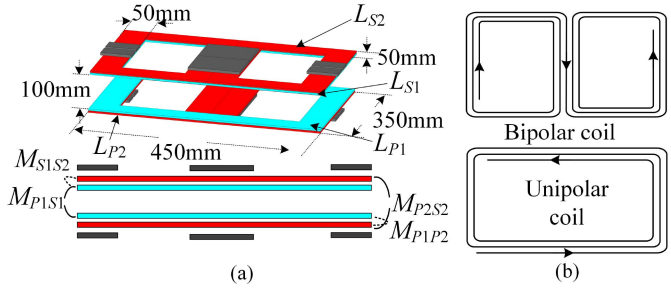

Fig. 6. (a) Three-dimensional view and (b) the magnetic coupler with decoupled four-coil structure of the proposed PPC-WiOBC system.

To compare the efficiency of the proposed PPC-WiOBC system with the conventional two-stage WOBC, the transfer efficiency of inverter to HV-Rec is defined as η_H, the transfer efficiency of inverter to LV-Rec is defined as η_A, and the efficiency of the auxiliary dc–dc converter is defined as $\eta_{\rm dc}$. Since the HV-Rec output voltage V_{oH}, the auxiliary dc–dc output V_{oL}, and the HVB voltage V_{oB} are connected in series, their relationship can be described as

$$V_{oH} + V_{oL} = V_{oB}. \tag{1}$$

The power ratio δ between the output power of the auxiliary dc–dc converter P_{oL} and the output power of the HV-Rec P_{oH} is defined as

$$\delta = \frac{P_{oL}}{P_{oH}} = \frac{V_{oL}}{V_{oH}} < 1. \tag{2}$$

The overall system efficiency η of the PPC-WiOBC system can be calculated as

$$\eta = \frac{\eta_{\rm dc}\eta_H\eta_A(1+\delta+\lambda)}{\eta_{\rm dc}\eta_A + \eta_H\delta + \lambda\eta_{\rm dc}\eta_H} \tag{3}$$

where λ is the power ratio between the output power of the AS and the HV-Rec.

Since $\lambda << 1$, (3) can be simplified as

$$\eta = \frac{\eta_{\rm dc}\eta_H\eta_A(1+\delta)}{\eta_{\rm dc}\eta_A + \eta_H\delta}. \tag{4}$$

The η_H and η_A are assumed to be 0.92 for analyzing the PPC high-efficiency constraint. According to (4), the system efficiency η contour versus $\eta_{\rm dc}$ and δ can be plotted, as shown in Fig. 5(b). As $\eta_{\rm dc}$ increases, η increases as well. Therefore, a low δ during the charging mode can significantly improve the effectiveness and efficiency of PPC, thereby enhancing the overall system efficiency. Even under the worst-case scenarios depicted in Fig. 5(b), where δ falls below 0.7 and an auxiliary dc–dc converter operates at a relatively low efficiency of only 60%, the PPC-WiOBC system still achieves an impressive efficiency exceeding 75%. Consequently, to ensure high system efficiency, a high-efficiency constraint design rule is established by defining the maximum power ratio $\delta_{\max} < 0.7$ as the high-efficiency constraint region. Within this range, the proposed system can operate with high efficiency.

III. Coupler, Control, and Parameters Design of Proposed PPC-WiOBC System

A. Magnetic Coupler With Decoupled Four Coil Structure

The magnetic coupler with a decupled four-coil structure is illustrated in Fig. 6, utilizing unipolar coils L_{P1} and L_{S1}, and bipolar coils L_{P2} and L_{S2}. This coil structure ensures negligible coupling between same side coils [28]. Specifically, L_{S1} is powered solely by L_{P1}, while L_{S2} is only powered exclusively by L_{P2}, which forms two mutually uncoupled power transmission paths to achieve CV output on both the HV-Rec and LV-Rec sides. To facilitate more efficient power transfer on PathI, L_{P1} and L_{S1} are positioned closer together, resulting in a relatively higher coupling coefficient.

B. Decoupled Four Coil Output Characteristics

In this article, a dual S/S compensation structure is applied to realize the CV output of both HV-Rec and LV-Rec sides. The coupling coefficient between L_{P1} and L_{S1} is given by $k_1 = M_{P1S1}/(L_{P1}\cdot L_{S1})^{1/2}$, and the coupling coefficient between L_{P2} and L_{S2} is given by $k_2 = M_{P2S2}/(L_{P2}\cdot L_{S2})^{1/2}$. The four coils of the magnetic coupler are compensated by series capacitors C_{P1}, C_{P2}, C_{S1}, and C_{S2} with resonant angular frequency ω

$$\omega = \frac{1}{\sqrt{L_{Px}\cdot C_{Px}}} = \frac{1}{\sqrt{L_{Sx}\cdot C_{Sx}}}, \qquad x = 1, 2. \tag{5}$$

The coils at the transmitter are connected in parallel. Since the two paths have no mutual inductance, the equation for their output voltages can be obtained from the loosely coupled transformer leakage inductance model as

$$V_{oH} = V_{\text{in}}\sqrt{\frac{L_{S1}}{L_{P1}}}, \qquad V_{oA} = V_{\text{in}}\sqrt{\frac{L_{S2}}{L_{P2}}}. \tag{6}$$

To improve the system efficiency, the zero-voltage switching (ZVS) turn-ON of the inverter at the transmitter side should be achieved, and the minimum L_{P1} and L_{P2} that satisfy the ZVS condition can be obtained by

$$\frac{V_{oH}}{4f_w k_1\sqrt{L_{P1}/L_{S1}}} + \frac{V_{oA}}{4f_w k_2\sqrt{L_{P2}/L_{S2}}} > 4C_{\text{oss}}\frac{V_{\text{in}}}{T_d} \tag{7}$$

where C_{oss} is the body capacitance of the MOSFET power switch.

The parameters of the dual S/S compensation structure that satisfy the ZVS condition can be determined by (5)–(7) to achieve a CV output, ensuring that there is no cross-interference between the HV-Rec and LV-Rec sides.

C. Operation of Bidirectional LC-LLC Multiresonant Isolated DC–DC Converter

The minimum output voltage of the auxiliary dc–dc converter must be as low as possible to meet the requirement for lower δ (better efficiency of PPC) and accommodate the wide voltage variation range of the HVB [29]. Consequently, the auxiliary dc–dc converter requires a wider voltage gain range compared to the dc–dc converter in the conventional WOBC.

The *LC-LLC* multiresonant dc–dc converter generates multiple resonance points through the effect of an antiresonant tank [30], and can even achieve zero voltage gain through slight frequency modulation. This feature significantly expands the output voltage gain range based on the *LLC* resonant dc–dc converter. In addition, the MOSFET switches of the converter can achieve ZVS turn-ON over the entire output voltage range by employing pulse frequency modulation (PFM), ensuring conversion efficiency.

Fig. 7(a) shows the bidirectional *LC-LLC* multiresonant dc–dc converter employed in this work. L_s and C_s form the series resonant tank, while L_p and C_p form the antiresonant tank. When the PPC-WiOBC system operates in charging mode, the multiresonant dc–dc converter operates in forward mode. When the PPC-WiOBC system operates in driving mode, an additional inductor L_{m2} is added as the magnetizing inductance, so that the dc–dc converter operates in the backward mode based on [29].

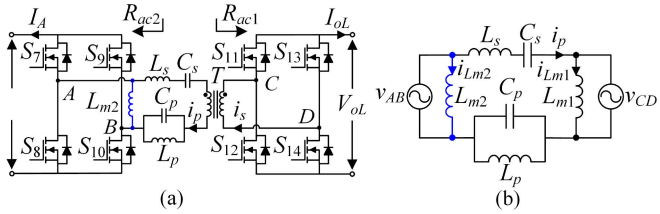

Fig. 7. (a) Bidirectional *LC-LLC* multiresonant DC–DC converter with an inductor L_{m2} and (b) its simplified equivalent circuit.

This additional L_{m2} creates a symmetric resonant tank, enabling bidirectional power transfer, as illustrated in Fig. 7(b).

The *LC-LLC* multiresonant dc–dc converter exhibits two series resonant frequencies, including the first series resonant frequency f_{r1} and the second series resonant frequency f_{r2}, which can be expressed as

$$f_{r1} = \sqrt{\frac{\varepsilon_1 - \sqrt{{\varepsilon_1}^2 - 4f_{rs}^2 f_{rp}^2}}{2}}, \varepsilon_1 = f_{rs}^2 + \lambda_{rs}^{-1} f_{rs} f_{rp} + f_{rp}^2 \tag{8}$$

$$f_{r2} = \sqrt{\frac{\varepsilon_2 - \sqrt{{\varepsilon_2}^2 - 4f_{rm}^2 f_{rp}^2}}{2}}, \varepsilon_2 = f_{rm}^2 + \lambda_{rm}^{-1} f_{rm} f_{rp} + f_{rp}^2. \tag{9}$$

The series and antiresonant tank impedances Z_s and Z_p are defined, respectively, as

$$Z_s = \left|\dot{Z_s}\right| = \left|j\left(\omega_s L_s - \frac{1}{\omega_s C_s}\right)\right| \tag{10}$$

$$Z_p = \left|\dot{Z_p}\right| = \left|\frac{j\omega_s L_p}{1-\omega_s^2 L_p C_p}\right|. \tag{11}$$

The theoretical forward and backward voltage gain G_F and G_B can be derived from the fundamental harmonic approximation, given as

$$G_F = \frac{nV_{oL}}{V_{oA}} = \frac{1}{\sqrt{\left(1+\frac{\xi}{\omega_s L_{m1}}\right)^2 + \left(\frac{\xi}{R_{ac1}}\right)^2}} \tag{12}$$

$$G_B = \frac{V_{oA}}{nV_{oL}} = \frac{1}{\sqrt{\left(1+\frac{\xi}{\omega_s L_{m2}}\right)^2 + \left(\frac{\xi}{R_{ac2}}\right)^2}} \tag{13}$$

$$\xi = Z_{rs}\left(F_x - \frac{1}{F_x}\right) - Z_{rp}\left(F_{rp} - \frac{1}{F_{rp}}\right)^{-1} \tag{14}$$

where $R_{\text{ac1}} = 8n^2 V_{oL}/I_{oL}\pi^2$, $R_{ac2} = 2V_{oA}/I_{oA}\pi^2$.

Based on (12) and (13), the theoretical curves of the forward and backward voltage gain G_F and G_B versus the normalized switching frequency F_x are shown in Fig. 8.

As shown in Fig. 8, the trends of the theoretical forward and backward voltage gain G_F and G_B curves are well-matched. In forward mode, when $f_{r2} \le f_s \le f_{r1}$, the secondary-side current i_s will naturally become zero while the primary-side resonant current i_p decreases to i_{Lm1}, S_{11}–S_{14} can be turned

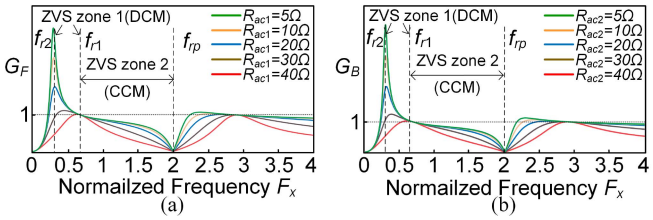

Fig. 8. Theoretical G_F and G_B curves versus F_x of the bidirectional *LC-LLC* multiresonant DC–DC converter under different $R_{\rm ac}$. (a) G_F. (b) G_B.

OFF by zero current switching (ZCS). During this interval, i_{Lm1} appears only in the transformer, while S_{11}–S_{14} operates in the discontinuous conduction mode. When $f_{r1} \leqslant f_s \leqslant f_{rp}$, there is no such interval, S_{11}–S_{14} cannot obtain ZCS turn-OFF. Therefore, the efficiency of ZVS zone 1 surpasses that of ZVS zone 2. Due to the antiresonance tank, the voltage gain in the high-frequency band decreases rapidly. This characteristic enables the dc–dc converter to output a lower output voltage, effectively enlarging the output voltage range.

To ensure high efficiency, the MOSFET switches must achieve ZVS turn-ON over the entire output voltage range. In forward mode, the MOSFET current equals the sum of the current i_{Lm1} of the inductor L_{m1} and the current i_{Lm2} of the additional inductor L_{m2}. The ZVS condition for the forward mode can be obtained from the energy conservation, and T_{dL} is the dead time of the *LC-LLC* multiresonant dc–dc converter

$$\frac{1}{2}(L_{m1}+L_r)I_{Lm1}^2+\frac{1}{2}L_{m2}I_{Lm2}^2 \geq 2C_{\rm oss}V_{oA}^2 \tag{15}$$

where $I_{Lm1} = (2G_F f_s\text{-}G_F f_{r1})V_{oA}/4L_{m1}f_s f_{r1}$, $I_{Lm2} = V_{oA}/4L_{m2}f_s$.

Therefore, the ZVS condition for forward mode can be obtained as

$$I_{Lm1}+I_{Lm2} \geq 2C_{\rm oss}(V_{oA}/T_{dL}). \tag{16}$$

The ZVS condition for the backward mode is equivalent to that of the forward mode, with the only distinction lying in the magnetic inductance value.

D. System Control Strategy

The proposed PPC-WiOBC system has two CV output paths for high and low-voltage sides, and there is no wireless communication between the transmitter and receiver sides. As shown in Fig. 9, the *LC-LLC* multiresonant dc–dc converter is using PFM. During charging mode, as illustrated by the blue line in Fig. 9(a), the output voltage V_{oB} and charging current I_{oC} are measured by using sensors, and the load R_{oB} can be calculated by using a divider. A simple PI controller corrects the difference between the feedback V_{oB} and its reference value V_{ref} for the CV stage and feedback I_{oC} and its reference value I_{ref} for the CC stage, forming the PFM generator for the MOSFET switches S_7–S_{10}. During driving mode, as illustrated in Fig. 9(b), the AS's voltage is measured by the sensor and corrects the difference between the feedback V_{oA} and its reference value V_{oAref} by PI

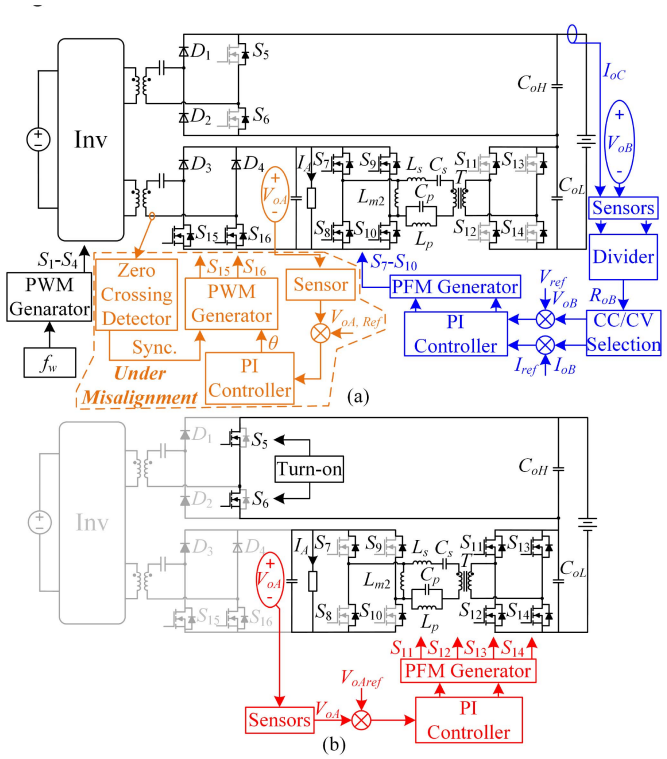

Fig. 9. Control diagram of the proposed PPC-WiOBC system. (a) Charging mode. (b) Driving mode.

controller, forming the PFM generator for the MOSFET switches S_{11}–S_{14}.

By setting the switching frequency of the dc–dc converter between f_{r2} and f_{rp}, a monotonically decreasing voltage gain curve can be obtained. The charging stage of the battery can be determined by comparing the calculated battery internal resistance with the point in the CC/CV curve, thereby the realization of CC to CV switching control is enabled.

E. Misalignment Tolerance

The topology proposed in this article mainly targets the static charging scenario of EVs under alignment states. However, in practical applications, minor misalignments are inevitable. To address this issue, this article introduces two switches (S_{15} and S_{16}) to form a semiactive rectifier (SAR) circuit. The operation waveforms are shown in Fig. 10. Zero-crossing detection of i_{S2} generates a synchronization signal for the pulsewidth modulation (PWM) generations. Angle θ is used to produce PWM driving signals for the SAR. The control block diagram under the misalignment condition is highlighted in orange, as shown in Fig. 9(a).

F. System Parameter Design

The parameters design flowchart of the PPC-WiOBC system is shown in Fig. 11, in which the design process commences by specifying the input requirements, including the WPT resonant angular frequency ω, dc input voltage $V_{\rm in}$, HVB voltage V_{oB},

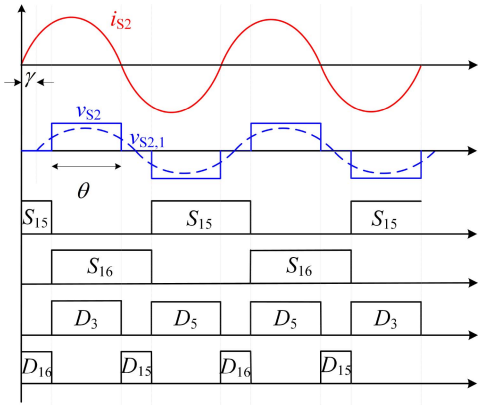

Fig. 10. Switching sequences and operation waveforms for the SAR.

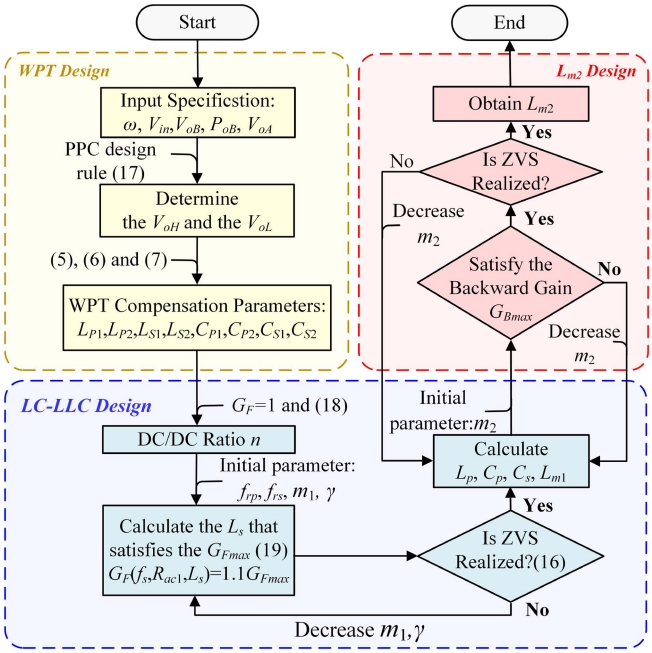

Fig. 11. Parameters design flowchart of the PPC-WiOBC system.

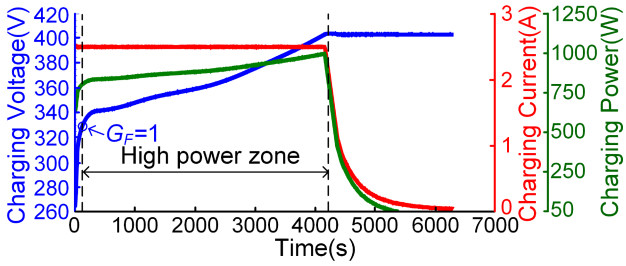

Fig. 12. Experimental HVB CC/CV charging curve.

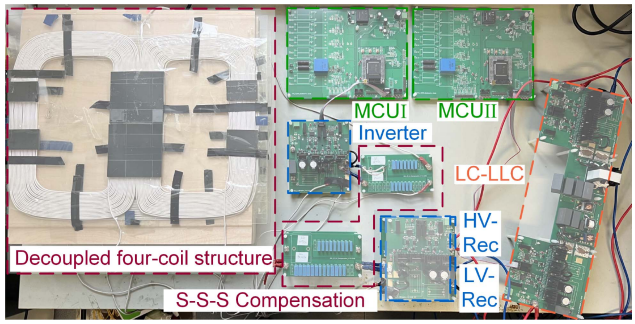

Fig. 13. Experimental prototype of the proposed PPC-WiOBC system.

battery power P_{oB}, and output voltage of the LV-Rec V_{oA}. These parameters serve as the foundation for the subsequent design stages.

The first stage involves the design of the WPT. The PPC design rule, as given in (1), is applied to determine the voltage series relationship of the HV-Rec output voltage V_{oH} and the output voltage of the auxiliary dc–dc converter V_{oL}. Then, according to the constraints of the high-efficiency region, (17) is further derived by using the maximum battery voltage $V_{oB\max}$ and the maximum power ratio $\delta_{\max}$, which can be used to determine the CV output value of V_{oH}, given as

$$V_{oH} + \delta_{\max} \cdot V_{oH} = V_{oB\max}. \tag{17}$$

With the design value of V_{oH}, the compensation parameters for the dual decoupled four-coil WPT system can be calculated by using (5), (6), and (7). These parameters include the primary and secondary inductances L_{P1}, L_{P2}, L_{S1}, L_{S2}, and compensation capacitances C_{P1}, C_{P2}, C_{S1}, and C_{S2} for both the high-voltage and low-voltage coil pairs.

Moving on to the design of the *LC-LLC* converter, the first step involves determining the dc–dc transformer turns ratio n by using (18) with the designed condition of $G_F = 1$. Then, the next step is to analyze the battery charging profile, which is shown in Fig. 12 for a 400 V EV battery with a 2.5 A charging current. During the charging stage, battery voltage rapidly increases until reaching almost 330 V, and then gradually rises until the charging process is completed. The voltage curves in Fig. 12 demonstrate that the high-power zone of charging lies within the battery voltage range of 330–402 V, necessitating the design to prioritize efficiency during this stage. Therefore, we operate $V_{oBfr1} = 330$ V at the frequency point f_{r1} where forward gain $G_F = 1$, ensuring that the high-power zone operates within the ZVS zone1 ($f_{r2} \leqslant f_s \leqslant f_{r1}$), thus guaranteeing efficient charging. The transformer turns ratio n of the *LC-LLC* converter can be calculated as

$$n = V_{oA}/(V_{oBfr1} - V_{oH}). \tag{18}$$

Then, the maximum switching frequency f_{rp} and series resonant frequency f_{rs} are initially determined based on the experimental conditions. High values for the coefficients m_1 and γ are initially chosen since increasing values of m_1 and γ will result in a decrease in resonant current i_p that reduces power losses of the resonant tank [30]. However, low values of resonant current i_p may hinder achieving the ZVS turn-ON condition of the *LC-LLC* converter. To address this trade-OFF, an iterative process is employed. First, as illustrated in (9), combining (12) and (14), the forward voltage gain G_F with f_s, $R_{\rm ac1}$, and L_s can

be obtained from

$$G_F(f_s, R_{\mathrm{ac1}}, L_s) = \frac{1}{\sqrt{\left(1+\frac{\xi}{2\pi L_s f_{rs} m_1 Fx}\right)^2 + \left(\frac{\xi}{R_{\mathrm{ac1}}}\right)^2}}. \tag{19}$$

Then, the inductance L_s is calculated using (19), which satisfies the maximum forward gain condition, $G_F(f_s, R_{\mathrm{ac1}}, L_s) = 1.1G_{F\max}$, where $G_{F\max}$ is the maximum forward gain during the charging process. The ZVS turn-ON condition, given by (16), is then evaluated. If the condition is not met, the values of m_1 and γ are iteratively reduced until the ZVS turn-ON condition is satisfied. Once the optimal values of m_1, γ, and L_s are determined, the remaining resonant tank parameters, such as L_p, L_s, C_p, C_s, and L_{m1} are calculated. The design process verifies that the complete ZVS condition (16) is realized across the entire operating range by adjusting parameters as necessary.

The final stage of the design process focuses on the backward mode operation, which is essential for bidirectional power flow during driving mode. Initially, a high value of the inductance ratio m_2 is chosen to minimize power losses. This value is then substituted into (13) to verify whether it satisfies the maximum backward gain constraint $G_{B\max}$, and then the ZVS turn-ON requirement. If the constraint is not met, the value of m_2 is iteratively reduced while re-evaluating the backward gain condition and the ZVS turn-ON requirement. Once both conditions are satisfied, the final value of the backward mode magnetizing inductance L_{m2} is determined.

The systematic design process ensures that the WPT and *LC-LLC* converter parameters are designed for high efficiency across the wide output voltage range requirement for EV battery charging. Moreover, it addresses the constraints for the bidirectional power flow of the *LC-LLC* converter during driving mode by considering the backward mode operation requirements.

IV. Experimental Verification

A. Experimental Prototype

To verify the output performance and high efficiency of the proposed PPC-WiOBC system, a scale-down experimental prototype was constructed in the laboratory, as shown in Fig. 13. The system parameters of the experimental prototype are shown in Table I. To facilitate a direct comparison between the actual WOBC based EV (as defined by SAEJ2954 standard) and the proposed scaled-down experimental prototype, relevant parameters are presented in Table II [31], [32]. In this experiment, an electronic load is used to emulate the HVB. The battery resistance R_{oB} ranges from 105.6 Ω to 160.8 Ω for CC charging and 160.8 Ω to 1608 Ω for CV charging. Moreover, the maximum system power reaches 1053 W. The experimental charging voltage V_{oB} and charging current I_{oC} versus battery resistance R_{oB} are shown in Fig. 14.

The system parameters of the PPC-WiOBC experimental prototype are shown in Table I. The coil in the magnetic coupler is made of 0.07 mm (diameter), and 714 strands of litz wire. The coil design is based on Fig. 6, with a rectangular shape of 450 mm in length and 350 mm in width, and the ferrite core material is PC95. In addition, the transmitter and receiver of the proposed system do not need to communicate, and TI DSP28335 is used as the microcontroller for the proposed PPC-WiOBC system.

TABLE I
Experimental System Parameters

System Parameters, Symbols	Values
Input voltage, V_{in}	170 V
Battery voltage, V_{oB}	264-402 V
HV-Rec output voltage, V_{oH}	248 V
LV-Rec output voltage, V_{oL}	16-154 V
Auxiliary system voltage, V_{oA}	48 V
Charging mode DC/DC voltage range, $V_{oLcharge}$	16-154 V
Driving mode DC/DC voltage range, $V_{oLdrive}$	264-402 V
Battery rated charging current, I_{oCmax}	2.5 A
Battery minimum charging current, I_{oCmin}	0.25 A
Auxiliary system current, I_A	1 A
LC-LLC DC/DC converter output power range	40-385 W
Inverter and Magnetic Coupler Parameters	
Operating frequency, f_w	85 kHz
Self-inductances L_{P1}, L_{P2}	205.3 μH, 557.6 μH
Self-inductances L_{S1}, L_{S2}	532.4 μH, 53.2 μH
Mutual inductances M_{P1S1}, M_{P2S2}	47.1 μH, 131.8 μH
Mutual inductances M_{P1P2}, M_{S1S2}	1.6 μH, 3.3 μH
Compensation capacitors C_{P1}, C_{P2}	28.4 nF, 8.6 nF
Compensation capacitors C_{S1}, C_{S2}	11 nF, 90.5 nF
Auxiliary DC/DC Converter Parameters	
Operating frequency range, f_s	31-200 kHz
Transformer windings turn ratio, n	2:3
Magnetizing inductance, L_{m1}	23.7 μH
Additional inductance, L_{m2}	20 μH
Series resonant-tank inductance, L_s	2.4 μH
Series resonant capacitor, C_s	1070.1 nF
Anti-resonant inductance, L_p	2.4 μH
Anti-resonant capacitor, C_p	267.5 nF
First series-resonant frequency, f_{r1}	68 kHz
Second series-resonant frequency, f_{r2}	31 kHz
Series-resonant frequency, f_{rs}	100 kHz
Anti-resonant frequency, f_{rp}	200 kHz

TABLE II
Specifications of the Actual WOBC Based EV and the Scaled-Down Experimental Prototype

Parameters	Actual	Scaled-down
Battery pack voltage	250-400 V	264-402 V
Charging power	7.7 kW	1 kW
Operating frequency	81.38-90 kHz	85 kHz

B. Steady-State Characteristics in Charging Mode and Driving Mode

The experimental steady-state output waveforms of the proposed system under CC and CV stages are shown in Fig. 15. The steady-state output waveforms under CC stage at a load of 140 Ω are shown in Fig. 15(a), where $\delta = 0.28$. The steady-state output waveforms under the CV stage at a load of 236 Ω are shown in Fig. 15(b), where $\delta = 0.43$. The V_{oA} can be kept at its reference value of 48 V. Due to the power loss in the WPT section, V_{oH} may exceed the rated value in Table I. However, precise output can still be achieved through the regulation of the auxiliary dc–dc converter. It can be observed that V_{oH}, V_{oL}, and V_{oB} conform to the voltage relationship described in (1).

The measured operational waveforms of the proposed system in charging mode under CC and CV stages are shown in Fig. 16.

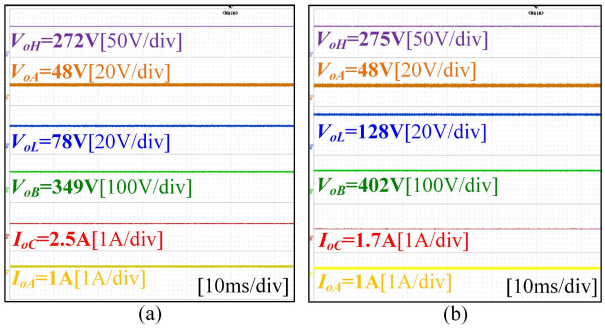

Fig. 15. Steady-state DC output waveforms in charging mode under. (a) CC stage. (b) CV stage.

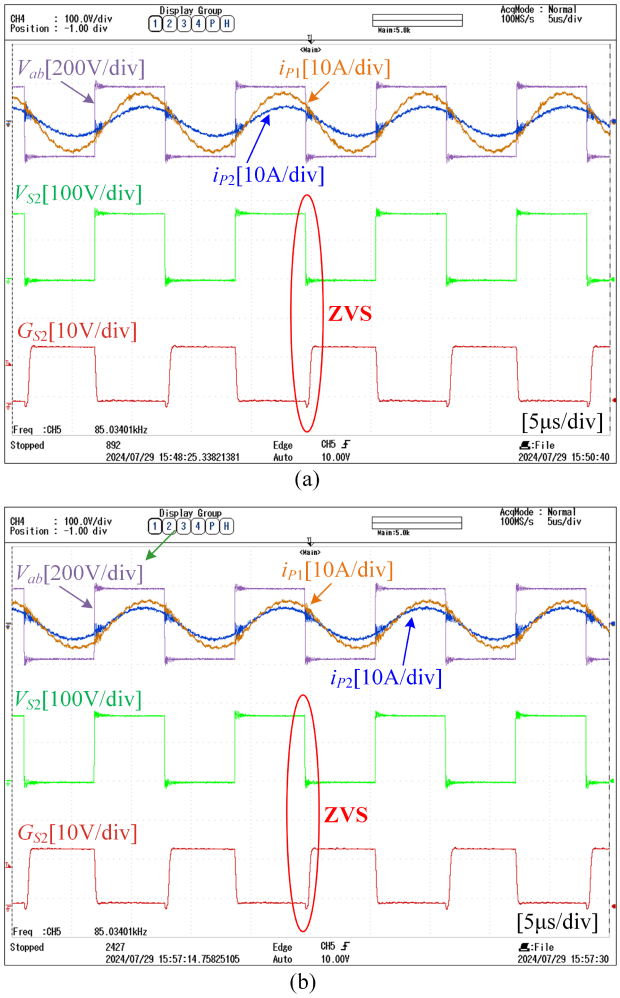

Fig. 16. Measured operational waveforms of the proposed PPC-WiOBC system in charging mode under. (a) CC stage. (b) CV stage.

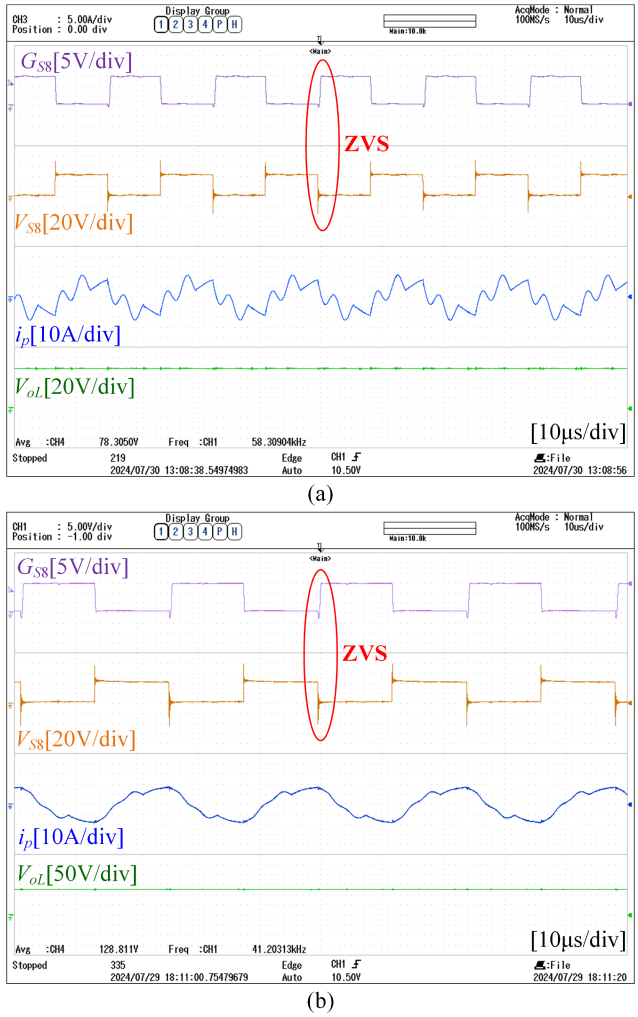

Fig. 17. Measured operational waveforms of the bidirectional *LC-LLC* multiresonant DC–DC converter in charging mode under. (a) CC stage. (b) CV stage.

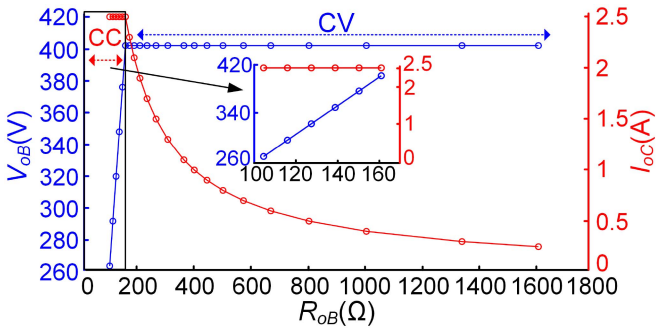

Fig. 14. Experimental charging voltage V_{oB} and charging current I_{oC} versus battery resistance R_{oB}.

It can be seen that the inverter voltage V_{ab} leads both currents i_{P1} and i_{P2}, indicating an inductive impedance and the MOSFET switches of the inverter can achieve ZVS turn-ON. The measured operational waveforms of the bidirectional *LC-LLC* converter in charging mode under CC and CV stages are shown in Fig. 17. It can be observed that the converter MOSFET switches can achieve ZVS turn-ON due to the resonant current i_p, verifying that this bidirectional *LC-LLC* multiresonant converter can maintain the resonance characteristics of the *LLC* converter.

In driving mode, the proposed system is only used to supply power to the AS for EV. The steady-state operational waveforms of the *LC-LLC* converter in driving mode are shown in Fig. 18. It

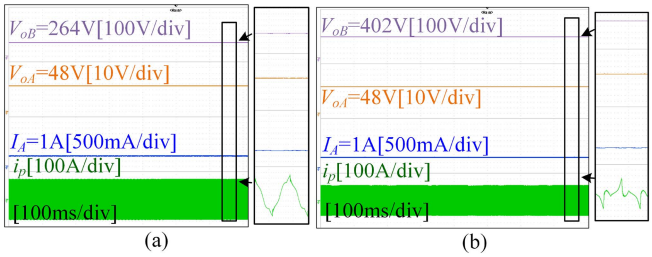

Fig. 18. Steady-state operational waveforms in the driving mode under. (a) $V_{oB} = 264$ V. (b) $V_{oB} = 402$ V.

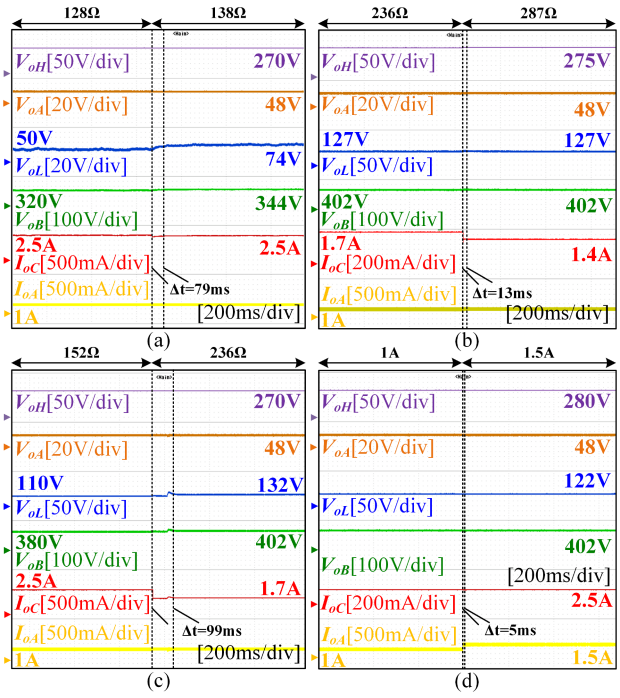

Fig. 19. Transient waveforms for different R_{oB} step changes under. (a) CC stage. (b) CV stage. (c) CC to CV stage. (d) AS step.

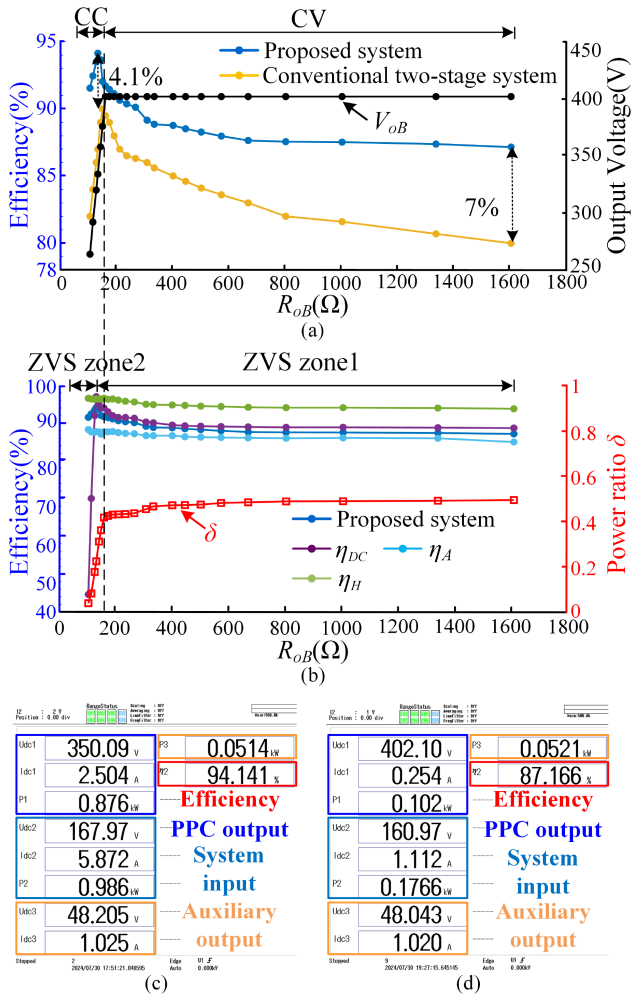

Fig. 20. Measured efficiency of the proposed PPC-WiOBC and the conventional two-stage wireless OBC with different R_{oB}. (a) System efficiency comparison. (b) Efficiency comparison of each part. (c) Maximum efficiency point. (d) Minimum efficiency point.

can be seen that the *LC-LLC* converter with additional inductor L_{m2} can achieve backward power transfer and meet the HVB voltage variation range from 264 to 402 V. Consequently, it can supply power to the AS during driving mode while maintaining the V_{oA} at its reference value of 48 V.

C. Transient Response Against Load Change

The transient waveforms for different battery resistance R_{oB} step changes under the CC stage, CV stage, and CC to CV stage are shown in Fig. 19. The waveforms under the CC stage with R_{oB} step changes from 128 to 138 Ω are shown in Fig. 19(a). After the R_{oB} step changes, the response time Δt of the system in the CC stage is 79 ms. The waveforms under the CV stage with R_{oB} step changes from 236 to 287 Ω are described in Fig. 19(b). It can be seen from Fig. 19(b) that the response time Δt of the system in the CV stage is 13 ms. Fig. 19(c) shows the waveform of the step change of R_{oB} from 152 to 236 Ω during the transition process of the CC to CV stage. It can be seen from Fig. 19(c) that the response time Δt of the system is 99 ms. The transition of the AS step corresponds to a change in the I_{oA} step from 1 A to 1.5 A, illustrated in Fig. 19(d). From Fig. 19(d), the response time Δt of the system is 5 ms. From Fig. 19, the control strategy used in the proposed system can achieve steady-state operation of the CC/CV charging profile and the transition from the CC to CV stage, which meets the application requirements.

D. System Efficiency Analysis

The system efficiency analysis compares the proposed PPC-WiOBC system with the conventional two-stage wireless OBC structure. Fig. 20(a) illustrates the measured efficiency of the proposed PPC-WiOBC and the conventional two-stage wireless OBC for CC/CV charging profile versus different R_{oB} values. Compared to the conventional two-stage wireless OBC, the proposed PPC-WiOBC system achieves a 4.1% higher efficiency at the maximum efficiency point in the CC charging stage. Even during the CV charging stage, the efficiency of the proposed system remains consistently high, with a 7% higher minimum efficiency compared to that of the conventional two-stage structure.

TABLE III
COMPARISONS SEMICONDUCTOR NUMBER AT THE EV SIDE, OUTPUT RANGE, AND EFFICIENCY

Reference	[33] (OBC+ LDC)	[8] (iOBC)	[34] (iOBC)	[35] (WOBC)	[36] (WiOBC)	[37] (WOBC)	[26] (PPC-WOBC)	[27] (PPC-WOBC)	This work (PPC-WiOBC)
Charging type	Plug-in	Plug-in	Plug-in	Wireless (Single-stage)	Wireless (Single-stage)	Wireless (Two-stage)	Wireless (PPC)	Wireless (PPC)	Wireless (PPC)
Number of *S* and *D*	10+12	10+3	12+0	4+0	8+0	4+8	2+8	1+9	6+10
		6+3	8+0		8+0				6+4
Operating mode	Charging	Charging	Charging	Charging	Charging	Charging	Charging	Charging	Charging
		Driving	Driving		Driving				Driving
Need relay	No	Yes	No	No	Yes	No	No	No	No
Charging profile	CC/CV	CC/CV	CC/CV	CC/CV	CC	CC/CV	CC/CV	CC/CV	CC/CV
Regulation capability	High	Medium	High	High	Low	High	Medium	Medium	High
Wireless feedback	——	——	——	Yes	No	Yes	No	No	No
Regulation power	Full	Full	Full	Full	Full	Full	Partial	Partial	Partial
Output power range	1-6.6 kW	1-6.6 kW	0.5-3.7 kW	28.8-288 W	0.8-1.2 kW	0.4-3.4 kW	216-432 W	54-250 W	0.1-1 kW
Output voltage range	250-450 V	380-710 V	240-420 V	32-72 V	185-296 V	240-410 V	36-72 V	60-84 V	264-402 V
Power ratio range	——	——	——	——	——	——	0.11-0.7	0.1-0.45	0.037-0.49
Efficiency	90-93.7%	92-97.7%	94-97.8%	60-90.2%	96%	75-89.6%	88-93%	79-89%	87.2-94.14%

Note: *S* and *D* denote switches and diodes, the shaded areas mean the desirable performance.

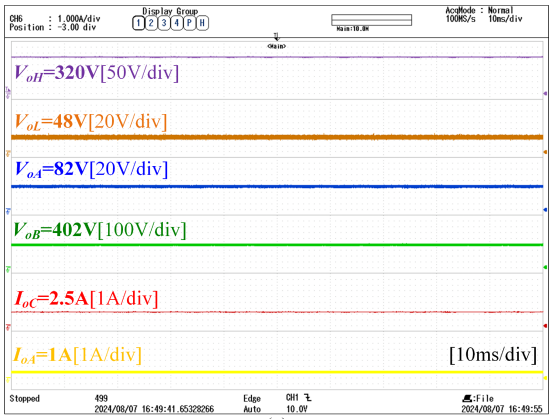

(a)

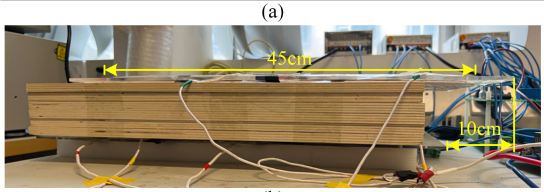

(b)

Fig. 21. Measured waveforms with horizontal misalignment. (a) Steady-state waveforms with a horizontal misalignment of 10 cm. (b) Misalignment photograph.

Fig. 20(b) illustrates the efficiency of each component, including system efficiency, high-voltage side efficiency (η_H), auxiliary side efficiency (η_A), and *LC-LLC* efficiency ($\eta_{\rm dc}$). It is evident that although the *LC-LLC* efficiency in the light-load region is significantly lower, even below 50%, the overall system efficiency remains consistently high. This can be attributed to the parameter design outlined in this work, which regulates the power ratio δ at a lower level during the CC charging stage, resulting in minimal power loss from *LC-LLC* and thereby maintaining an elevated overall efficiency. During the CV charging stage, the power ratio is controlled to be less than 0.7 (0.038–0.49), and the system efficiency is improved by 7% at the end of the charging process. The high efficiency of the whole charging process can be maintained as long as the power ratio δ of the PPC is kept within the high-efficiency constraint range ($\delta_{\max} < 0.7$).

The proposed PPC-WiOBC system achieves a maximum efficiency of 94.14% and a minimum efficiency of 87.1%, as illustrated in Fig. 20(c) and (d), respectively. This consistent high efficiency throughout the charging process, highlights the significant advantage of the proposed system over the conventional two-stage WOBC.

E. Misalignment Issue

Meanwhile, an experiment on horizontal misalignment has constructed and presented the experimental waveform under full load conditions in Fig. 21. As depicted in Fig. 21(a), following SAR regulation, the AS voltage V_{oA} stabilized at 48 V, while V_{oH} increased to 320 V. Even after regulation by *LC-LLC*, the output voltage V_{oB} remained at the reference value of 402 V. Fig. 21(b) shows a photograph of a coil with a horizontal misalignment of 10 cm.

F. Comparison With the State-of-the-Art Designs

Table III presents a brief comparison of the proposed PPC-WiOBC and previous works. The key parameters, including semiconductor number, operating mode, charging profile, regulation capability, feedback, power regulation mode, output

range, and efficiency are summarized. It demonstrates clear benefits in the regulation range (power and voltage) and efficiency in wireless charging applications. Furthermore, despite the nondominant presence of semiconductors in this work, it offers two modes of charging and driving without requiring additional LDC. In comparison to existing WOBCs with PPC structure, the range of power ratio δ is wider, the minimum power ratio is lower, and efficiency is higher due to the reasonable parameter design in the proposed PPC-WiOBC system.

V. Conclusion

This article proposes a WiOBC system for EVs based on PPC to handle wide load ranges during the CC/CV charging profile while maintaining high efficiency. In comparison to the conventional two-stage WOBC, most power flows directly to the high-voltage battery, while a small portion undergoes two-stage regulation, thus improving the system's overall efficiency and reducing regulation power rating requirements. Unlike other PPC-based WOBCs, the proposed system allows the HVB and AS to be simultaneously powered by the charging station, Furthermore, the auxiliary dc–dc converter can be controlled to operate in backward mode, enabling the PPC-WiOBC system to function in driving mode without requiring an additional LDC. By introducing an *LC-LLC* multiresonant converter with a wide load range and setting PPC under high-efficiency constraints, an overall system parameter design process provides high efficiency across the entire load range with a lower application threshold. To validate the approach, a 1 kW experimental prototype was designed using the proposed parameter design flowchart. Experimental results demonstrate a maximum efficiency of 94.14% and a minimum efficiency of 87.1%, outperforming the conventional two-stage WOBC schemes. Especially, the maximum efficiency increased by 4.1%, while the light-load region with efficiency improved by 7%.

References

[1] A. Emadi, *Advanced Electric Drive Vehicles*. Boca Raton, FL, USA: CRC Press, 2014.

[2] I. Aghabali, J. Bauman, P. J. Kollmeyer, Y. Wang, B. Bilgin, and A. Emadi, "800–V electric vehicle powertrains: Review and analysis of benefits, challenges, and future trends," *IEEE Trans. Transp. Electrific.*, vol. 7, no. 3, pp. 927–948, Sep. 2021.

[3] G. Broadbent, G. Metternicht, and D. Drozdzewski, "An analysis of consumer incentives in support of electric vehicle uptake: An australian case study," *World Elect. Veh. J.*, vol. 10, no. 11, pp. 1–15, Mar. 2019.

[4] X. Zhou et al., "A high–efficiency high–power–density on–board low–voltage DC–DC converter for electric vehicles application," *IEEE Trans. Power Electron.*, vol. 36, no. 11, pp. 12781–12794, Nov. 2021.

[5] S.-G. Jeong, Y.-S. Jeong, J.-M. Kwon, and B.-H. Kwon, "A soft–switching single–stage converter with high efficiency for a 3.3–kW on–board charger," *IEEE Trans. Ind. Electron.*, vol. 66, no. 9, pp. 6959–6967, Sep. 2019.

[6] C. Jung, "Power up with 800–V systems: The benefits of upgrading voltage power for battery–electric passenger vehicles," *IEEE Electrific. Mag.*, vol. 5, no. 1, pp. 53–58, Mar. 2017.

[7] Y. Zhang et al., "Leakage current issue of non–isolated integrated chargers for electric vehicles," in *Proc. IEEE Energy Convers. Congr. Expo.*, 2018, pp. 1221–1227.

[8] D.-W. Lee, B.-S. Lee, J.-H. Ahn, J.-Y. Kim, and J.-K. Kim, "New combined OBC and LDC system for electric vehicles with 800 V battery," *IEEE Trans. Ind. Electron.*, vol. 69, no. 10, pp. 9938–9951, Oct. 2022.

[9] Y. Tang, J. Lu, B. Wu, S. Zou, W. Ding, and A. Khaligh, "An integrated dual–output isolated converter for plug–in electric vehicles," *IEEE Trans. Veh. Technol.*, vol. 67, no. 2, pp. 966–976, Feb. 2018.

[10] R. Hou and A. Emadi, "A primary full–integrated active filter auxiliary power module in electrified vehicles with single–phase onboard chargers," *IEEE Trans. Power Electron.*, vol. 32, no. 11, pp. 8393–8405, Nov. 2017.

[11] S. Jayalath and A. Khan, "Design, challenges, and trends of inductive power transfer couplers for electric vehicles: A review," *IEEE J. Emerg. Sel. Topics Power Electron.*, vol. 9, no. 5, pp. 6196–6218, Oct. 2021.

[12] D. Patil, M. K. McDonough, J. M. Miller, B. Fahimi, and P. T. Balsara, "Wireless power transfer for vehicular applications: Overview and challenges," *IEEE Trans. Transp. Electrific.*, vol. 4, no. 1, pp. 3–37, Mar. 2018.

[13] V. Cirimele, M. Diana, F. Freschi, and M. Mitolo, "Inductive power transfer for automotive applications: State–of–the–art and future trends," *IEEE Trans. Ind. Appl.*, vol. 54, no. 5, pp. 4069–4079, Sep./Oct. 2018.

[14] Z. Huang, S.-C. Wong, and C. K. Tse, "An inductive–power–transfer converter with high efficiency throughout battery–charging process," *IEEE Trans. Power Electron.*, vol. 34, no. 10, pp. 10245–10255, Oct. 2019.

[15] I.-W. Iam et al., "Constant–frequency and noncommunication–based inductive power transfer converter for battery charging," *IEEE J. Emerg. Sel. Topics Power Electron.*, vol. 10, no. 2, pp. 2147–2162, Apr. 2022.

[16] E. L. Carvalho, C. A. Felipe, L. V. Bellinaso, C. M. d. O. Stein, R. Cardoso, and L. Michels, "Asymmetrical–PWM DAB converter with extended ZVS/ZCS range and reduced circulating current for ESS applications," *IEEE Trans. Power Electron.*, vol. 36, no. 11, pp. 12990–13001, Nov. 2021.

[17] W. Liu, K. T. Chau, C. H. T. Lee, C. Jiang, W. Han, and W. H. Lam, "A wireless dimmable lighting system using variable–power variable–frequency control," *IEEE Trans. Ind. Electron.*, vol. 67, no. 10, pp. 8392–8404, Oct. 2020.

[18] I.-W. Iam, C.-K. Choi, C.-S. Lam, P.-I. Mak, and R. P. Martins, "A constant–power and optimal–transfer–efficiency wireless inductive power transfer converter for battery charger," *IEEE Trans. Ind. Electron.*, vol. 71, no. 1, pp. 450–461, Jan. 2024.

[19] W. Liu, K. T. Chau, C. H. T. Lee, C. Jiang, W. Han, and W. H. Lam, "A wireless dimmable lighting system using variable–power variable–frequency control," *IEEE Trans. Ind. Electron.*, vol. 67, no. 10, pp. 8392–8404, Oct. 2020.

[20] S. Ann and B. K. Lee, "Analysis of impedance tuning control and synchronous switching technique for a semibridgeless active rectifier in inductive power transfer systems for electric vehicles," *IEEE Trans. Power Electron.*, vol. 36, no. 8, pp. 8786–8798, Aug. 2021.

[21] Z. Huang, S.-C. Wong, and C. K. Tse, "An inductive-power-transfer converter with high efficiency throughout battery-charging process," *IEEE Trans. Power Electron.*, vol. 34, no. 10, pp. 10245–10255, Oct. 2019.

[22] M. Kim, D.-M. Joo, and B. K. Lee, "Design and control of inductive power transfer system for electric vehicles considering wide variation of output voltage and coupling coefficient," *IEEE Trans. Power Electron.*, vol. 34, no. 2, pp. 1197–1208, Feb. 2019.

[23] J. H. R. Enslin and D. B. Snyman, "Combined low-cost, high-efficient inverter, peak power tracker and regulator for PV applications," *IEEE Trans. Power Electron.*, vol. 6, no. 1, pp. 73–82, Jan. 1991.

[24] H. Chiu, Y. Lo, P. Tseng, and Y. Liu, "High–efficiency battery charger with cascade output design," *IET Power Electron.*, vol. 7, no. 7, pp. 1725–1735, Jan. 2014.

[25] G. Fan, X. Wu, T. Liu, and Y. Xu, "High–efficiency high–density MHz cellular DC/DC converter for on–board charger," *IEEE Trans. Power Electron.*, vol. 37, no. 12, pp. 15666–15677, Dec. 2022.

[26] W. Xiong, Z. Yan, D. Tang, W. Zhou, and R. Mai, "A hybrid topology IPT system with partial power processing for CC-CV charging," *IEEE Trans. Power Electron.*, vol. 39, no. 1, pp. 1701–1712, Jan. 2024.

[27] X. Wang, L. He, J. Xu, C.-K. Lee, and C. K. Tse, "Power–spilt–based wireless charging system with communication–free coordination control," *IEEE Trans. Power Electron.*, vol. 38, no. 2, pp. 2754–2767, Feb. 2023.

[28] Y. Li, T. Lin, R. Mai, L. Huang, and Z. He, "Compact double-sided decoupled coils-based WPT systems for high-power applications: Analysis, design, and experimental verification," *IEEE Trans. Transp. Electrific.*, vol. 4, no. 1, pp. 64–75, Mar. 2018.

[29] T.-T. Le, R. M. Hakim, and S. Choi, "A high–efficiency bidirectional single–stage AC–DC converter under wide voltage range for fast chargers," *IEEE Trans. Power Electron.*, vol. 38, no. 4, pp. 4945–4956, Apr. 2023.

[30] T. Mishima, H. Mizutani, and M. Nakaoka, "A sensitivity–improved PFM LLC resonant full–bridge DC–DC converter with LC antiresonant circuitry," *IEEE Trans. Power Electron.*, vol. 32, no. 1, pp. 310–324, Jan. 2017.

[31] *Electric vehicle wireless power transfer (WPT) systems– Part 1: General requirements*, IEC 61980-1:2020, 2020. [Online]. Available: https://webstore.iec.ch/en/publication/31657
[32] *Wireless Power Transfer for Light Duty Plug-in/Electric Vehicles and Alignment Methodology*. Warrendale, PA, USA: SAE, 2019.
[33] J.-Y. Lee and H.-J. Chae, "6.6-kW onboard charger design using DCM PFC converter with harmonic modulation technique and two-stage DC/DC converter," *IEEE Trans. Ind. Electron.*, vol. 61, no. 3, pp. 1243–1252, Mar. 2014.
[34] G. Yu and S. Choi, "An effective integration of APM and OBC with simultaneous operation and entire ZVS range for electric vehicle," *IEEE Trans. Power Electron.*, vol. 36, no. 9, pp. 10343–10354, Sep. 2021.
[35] Y. Jiang et al., "Phase-locked loop combined with chained trigger mode used for impedance matching in wireless high power transfer," *IEEE Trans. Power Electron.*, vol. 35, no. 4, pp. 4272–4285, Apr. 2020.
[36] Y. Zhang et al., "An integrated electric vehicle charging system of wireless power transfer and auxiliary power module with shared converter and magnetic coupler," *IEEE Trans. Ind. Electron.*, vol. 71, no. 9, pp. 10414–10421, Sep. 2024.
[37] M. Kim, D.-M. Joo, and B. K. Lee, "Design and control of inductive power transfer system for electric vehicles considering wide variation of output voltage and coupling coefficient," *IEEE Trans. Power Electron.*, vol. 34, no. 2, pp. 1197–1208, Feb. 2019.

Muxing Wu (Student Member, IEEE) received the B.Sc. degree in electrical and intelligent engineering from Xiangtan University, Xiangtan, China, in 2018, and the M.Sc. degree in electrical engineering from Yanshan University, Qinhuangdao, China, in 2022. He is currently working toward the Ph.D. degree in electrical and computer engineering from the University of Macau (UM), Macau, China.

His current research interests include wireless power transfer and resonant converter.

Io-Wa Iam received the B.Sc. and Ph.D. degrees in electrical and computer engineering from the University of Macau (UM), Macau, China, in 2020 and 2023, respectively.

He is currently a Research Assistant Professor with the State Key Laboratory of Analog and Mixed-Signal VLSI and the Institute of Microelectronics, UM. His current research interests include power electronics and wireless power transfer.

Dr. Iam was the recipient of the Macao Science and Technology R&D Award for Postgraduates (Ph.D. Level) in 2024. In 2019, he was awarded the "Best Track Paper Award" in APPEEC 2019.

Chi-Seng Lam (Senior Member, IEEE) received the Ph.D. degree in electrical and electronics engineering from the University of Macau (UM), Macau, China, in 2012.

He completed the Clare Hall Study Programme with the University of Cambridge, Cambridge, U.K., in 2019. In 2013, he was a Postdoctoral Fellow with The Hong Kong Polytechnic University, Hong Kong. He is currently an Associate Professor with the State Key Laboratory of Analog and Mixed-Signal VLSI and the Institute of Microelectronics, UM, and also with the Department of Electrical and Computer Engineering, Faculty of Science and Technology, UM. He has coauthored or coedited five books and more than 200 technical journals and conference papers. He holds six U.S. and seven Chinese patents. His research interests include power quality compensators, photovoltaic energy generation system, power management integrated circuits, and wireless power transfer.

Dr. Lam was the recipient or corecipient of the IEEE PES Chapter Outstanding Engineer Award in 2016, the Gold Medal of the 48th Geneva International Exhibition of Inventions in 2023, and the Macao Science and Technology Invention Awards (Third Class, Second Class and Third Class) in 2014, 2018, and 2024 respectively. He is currently the Chair of the Young Professionals in Circuits and Systems of IEEE CASS, Founding Chair of the IEEE Macau IES Chapter, and the Secretary of the IEEE IES Technical Committee on Power Electronics. He is currently an Associate Editor for IEEE TRANSACTIONS ON POWER ELECTRONICS, IEEE TRANSACTIONS ON INDUSTRIAL ELECTRONICS, the IEEE JOURNAL OF EMERGING AND SELECTED TOPICS IN POWER ELECTRONICS, the *IEEE Open Journal of the Industrial Electronics Society*, and the IEEE ACCESS. He was awarded 2021 IEEE Access Outstanding Associate Editor and the 2022 IEEE TRANSACTIONS ON INDUSTRIAL ELECTRONICS Distinguished Reviewer.